Regular Article

Strain rate and triaxiality effects on the dynamic ductile damage of DOMEX 355MC

M.P. Weyer, T.J. Cloete[a], and R.A. Govender

Blast Impact and Survivability Research Unit (BISRU), Department of Mechanical Engineering, University of Cape Town, Private Bag X3, Rondebosch 7701, South Africa

Abstract. The effect of strain rate on the ductile fracture of DOMEX 355MC, a high strength low alloy steel, is investigated using notched specimens loaded in uniaxial tension at quasi-static and high strain rates. The high strain rate tests are conducted on a tensile Split Hopkinson Bar (SHB), which incorporates a novel mechanism for tensile loading using an otherwise standard gas gun. Furthermore, the Tensile SHB uses a novel "fir-tree" gripping system which permits rapid changing of specimens, minimises slack between specimens and the bar and prevents slippage. The experiments were simulated in explicit FEA using a material model that incorporates temperature and rate sensitive plasticity, to identify the local strain at fracture. The intent of the simulations is to extend the pragmatic approach of Wierzbicki and co-authors [Int. J. Mech. Sci. **46**, 81 (2004); Study on the effect of the third stress invariant on ductile fracture, Tech. Rep. 151, 2006; Int. J. Plast. **24**, 1071 (2008)], who studied the effect of triaxiality and Lode angle on strain at fracture at quasi-static rates, to a higher strain rates. The experiments conducted had a Lode angle of approximately 1 prior to the onset of necking. The strain at fracture for DOMEX 355MC decreased as strain rate increased, for the range of strain rates and Lode angles which were studied.

1 Introduction

The study of ductile fracture in a crack-free body at a macroscopic level is a challenging problem, as there is limited consensus as to what parameters are required, or which models to utilise, to accurately predict the onset of fracture over a wide range of loading conditions. The driving mechanisms of ductile fracture, such as void growth and coalescence, typically occur at microscopic scales [4–6]. Consequently, it is not feasible to resolve microscopic damage mechanisms in simulations on a macroscopic scale. Material models that are able to resolve micro-damage are infeasible for simulations on a macroscopic scale. Therefore, several continuum models [1,3,7,8] have been developed where the effect of microscopic damage is captured using damage parameters, while not explicitly resolving the actual damage mechanisms.

---

[a] e-mail: trevor.cloete@uct.ac.za

Early, continuum mechanics-based models by McClintock [4], Rice and Tracey [5], and Gurson [6] suggest that the strain at fracture is closely related to the hydrostatic tension at the location of fracture, as an increase in hydrostatic tension encourages the growth of voids. The commonly used Rice and Tracey model describes the relationship between strain at fracture and hydrostatic tension as:

$$\epsilon_f = C \exp\left(-\frac{3}{2}\eta\right), \tag{1}$$

where η is the stress triaxiality, which is defined by:

$$\eta = \frac{-p}{\bar{\sigma}}. \tag{2}$$

The triaxiality describes the ratio between the hydrostatic pressure, p, and the von Mises flow stress, $\bar{\sigma}$. Equation (1) was modified by Johnson and Cook [7] to create an empirical damage model, which included additional strain rate and temperature effects observed in OFHC Copper, Armco iron and 4340 alloy steel. However, Bao and Wierzbicki [1] later showed that experimental data for 2024-T351 aluminium alloy did not conform to a monotonic relationship between strain at failure and triaxiality, and proposed a piecewise function to describe the relationship between the strain at failure and the triaxiality.

Bao and Wierzbicki argued that the fracture mechanisms are predominantly void growth and shear decohesion in the regions of high and low triaxialities respectively. Thus two different functions are used to describe the strain at failure in these regions, and a third to capture the region where the failure mode is a combination of the two mechanisms. This work is significant, as it shows that the stress triaxiality alone does not accurately describe the damage in a body over a large range of loading conditions. Subsequently, work by Xue and Wierzbicki [8], as well as Bai and Wierzbicki [3], showed that a second parameter could be used to define the fracture locus using a single function. This parameter is the Lode angle θ, given by:

$$\cos(3\theta) = \frac{27}{2}\frac{J_3}{\bar{\sigma}^3}, \tag{3}$$

where J_3 is the third deviatoric stress invariant (for further explanation see Bai and Wierzbicki [9], or Weyer [10]). A normalised form of the Lode angle is given as:

$$\bar{\theta} = 1 - \frac{6\theta}{\pi}. \tag{4}$$

While several investigations have been published concerning the effects of strain rate on the strain at failure [7,11–14], there is currently no definitive model describing the effect of strain rate on ductile damage. While the aforementioned investigations all indicate that an increase in strain rate results in an increase in elongation for ductile metals, other studies (for example [15]) observed a decrease in elongation in high strain rate tensile Hopkinson bar tests. As noted by Verleysen and Peirs [16], strain localisation means that decreased global elongation does not necessarily mean decreased local strain at fracture, which may contribute to the lack of consensus in the literature on this matter.

The aim of this paper is to present the results of experiments performed over a range of different strain rates, such that a damage model can be calibrated to the data, and the effect of strain rate on ductile fracture can be studied. The specimen material in this investigation is DOMEX 355MC, which is a hot rolled, high strength low alloy
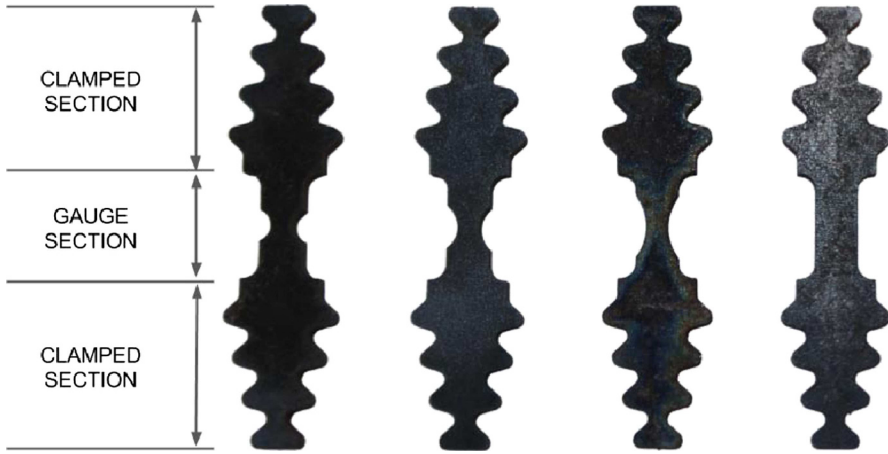
Fig. 1. The notched and straight specimens.

steel, produced by SSAB. This material, as well as other DOMEX alloys, have been the subject of several blast loading investigations in the authors' laboratory (for example [17,18]), as candidate materials for landmine protected vehicles. Hence the rate dependency of its plastic response and fracture are of interest both to academic research and industrial applications. For the purpose of this paper, the experiments focused on the region of $0.5 \lesssim \bar{\theta} \lesssim 1$ (prior to necking) and $\eta \geq 0.3$. This was to determine the effect of strain rate on the damage behaviour of the material, rather than the effect of the Lode parameter, under similar conditions to which ductile tearing was observed in the blast loading studies [17,18].

2 Specimen and apparatus design

In order to perform uni-axial tensile experiments over a range of triaxialities, straight and notched specimens are used as shown in Figure 1. SSAB DOMEX 355MC plate steel of 3 mm thickness was used with notch radii of R5.0 mm, R2.5 mm and R1.5 mm. The notches increase the triaxiality at the center of the specimens. For compatibility with the Split Hopkinson Bar (SHB) apparatus, the specimens are small (the gauge section of each specimen is 10 mm × 4 mm, with a minimum width of 2 mm for the notched specimens), and have a novel "fir-tree" shaped clamped section which fits in a threaded clamp designed for use with a tensile SHB apparatus. This design is discussed in Section 2.1. For consistency, the same specimen and clamp design was used for both the dynamic and quasistatic tests. The specimens are tested at a dynamic strain rate using the tensile SHB, and two quasistatic strain rates using a Zwick tensile testing machine at 0.6 mm/min and 100 mm/min. The corresponding strain rates were averaged over the strain in a similar manner to the average triaxiality defined by Bao and Wierzbicki [1]:

$$\bar{\bar{\varepsilon}} = \frac{1}{\varepsilon_f} \int_0^{\varepsilon_f} \dot{\varepsilon} \mathrm{d}\varepsilon. \tag{5}$$

The average strain rates were determined via simulation, and are shown in Table 1.

Table 1. The strain-averaged strain rates for each of the tests in s^{-1}.

Test regime	Straight	Notch R5.0 mm	Notch R2.5 mm	Notch R1.5 mm
0.6 mm/min	0.006	0.008	0.009	0.009
100 mm/min	0.7	1.3	1.4	1.3
SHB	3121	5416	6137	6022

2.1 "Fir-tree" specimens and clamps

A novel feature of the tensile SHB apparatus used in this work is the clamping mechanism used to secure the specimens to the bars, as shown in Figure 2. Unlike a compressive SHB specimen, tensile specimens must be securely fastened to the input and output bars in order to transfer a tensile load. To achieve this for plate steel specimens, the "fir-tree" specimen and clamp has been developed at BISRU.

The clamps, made from Ti-6Al4V, have the form of a split tapered thread with internal recesses that match the "fir-tree" ends of the specimen (see Fig. 2) and collet grooves that allow the clamps to expand slightly and "snap" onto a specimen for ease of handling. The clamps were not made from the same alloy as the bars (Al-7075) due to concerns around plastic deformation of the clamps in the thin collet sections, and the possibility of binding between the bars and clamps. Ti-6A4V avoided these concerns, without introducing the severe impedance mismatch associated with steel clamps. Using a custom tool, the specimen/clamp assembly is screwed into a matching tapered thread in the bar ends, where the taper causes the clamps to tighten onto the specimen in a manner analogous to a four jaw chuck.

The primary advantage of using a tapered thread is the ability to produce a large clamping force due to hoop stresses generated in the bar material around the threads. This removes the need for additional parts, such as clamp bolts, and minimizes the mass of the clamps and the material removed from the bar ends, all of which reduce the impedance mismatch due to the clamps. Furthermore, the tapered shape allows for a more gradual stress wave transfer at the threaded interface than a uniform thread provides, which contributes to an improved signal quality. The large clamping forces, in conjunction with the tapered shape of the fir-tree lobes, ensure that each lobe is properly seated in the clamp when tightened. This automatically compensates for small tolerance variations in the specimen manufacture by eliminating any "play" or "backlash" between the specimen and the clamps. This, in turn, promotes equal loading between all the lobes, which ensures that the specimen will deform in the gauge section and not in the clamped section.

In addition to the above, the tapered thread design has practical advantages for routine testing as it requires no gluing, is self centring and requires significantly fewer turns to fully tighten than is the case for a uniform thread. These features allow for a turn-around time between tests of a few minutes, while ensuring axial alignment of the specimen and bars. Lastly, the design is cost effective, as specimens can be EDM wire-cut from stacked plates.

2.2 Tensile striker configuration

The novel tensile striker configuration used for this work has been developed at BISRU to allow a conventional SHB apparatus to be adapted for tensile SHB testing with only minor modifications required to the gas gun barrel and input bar. A tensile pulse is generated using a tubular striker that impacts upon a collar on the input bar (see Fig. 3). However, unlike similar tensile SHB setups, the striker slides over the gas gun barrel, in addition to the input bar. The striker is impedance matched to the

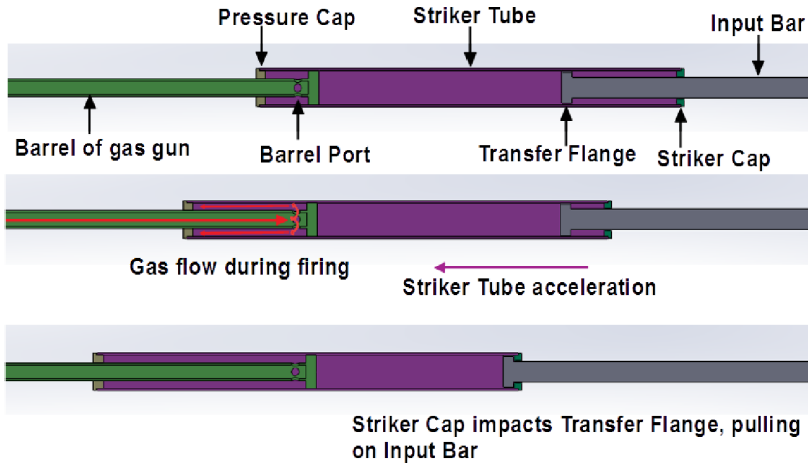**Fig. 2.** The clamps used to secure the specimens in the Split Hopkinson Bar.

Fig. 3. A schematic of the tensile striker adaptor mechanism.

input bar and the inner diameter has a close running fit to a "plug" that seals the end of the barrel.

Upon firing, pressurised air escapes through the barrel port of the barrel, filling the cavity between the barrel and striker, and is trapped by a "pressure cap" threaded into the rear end of the striker, which provides a seal between the barrel and the striker. The force on the pressure cap accelerates the striker backwards, thus "pulling" the striker tube off the input bar, until a "striker cap", threaded into the front side of the striker, impacts upon the collar threaded onto the input bar to generate the tensile pulse.

An advantage of the design is that a conventional compressive SHB apparatus can be adapted to use the tensile striker with minor modifications to the gas gun barrel and the input bar. The input and output bar lengths are 3.3 m and 2.25 m respectively, and the diameters are 19.09 mm and 19.9 mm respectively. Both bars are made from 7075-T6 aluminium. Figure 4 shows typical incident, reflected and transmitted waves that have been shifted to the bar-specimen interfaces. The new tensile striker produces repeatable trapezoidal waves with negligible overshoot, that are easily pulse smoothed by application of suitable pliable material at one of the collars.

3 Numerical modelling

In order to calibrate the chosen damage model, parallel numerical simulations were performed in LS-DYNA to infer the damage parameters at the point of fracture. This
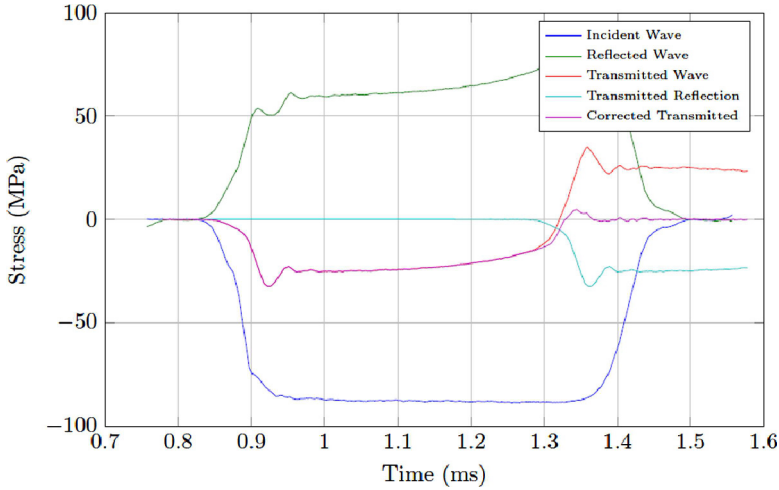
Fig. 4. Typical incident, reflected and transmitted waves for the new striker mechanism.

study does not use a coupled damage-plasticity model, as it simply seeks to extend the pragmatic approach of Bao and Wierzbicki [19] in quasi-static fracture to a series of dynamic tests.

3.1 Plasticity model

The experimental data obtained from the straight specimen tests was used to calibrate a plasticity model (see Fig. 7), after which each test was simulated in order to determine the triaxiality, strain rate and plastic strain in the element where failure initiates. The chosen plasticity model is that proposed by Zhao [20], which incorporates strain rate and temperatures effects, as described by:

$$\bar{\sigma} = h(\varepsilon, \dot{\varepsilon}) \cdot f(T), \tag{6}$$

$$h(\varepsilon, \dot{\varepsilon}) = A + B\varepsilon^n + (C - D\varepsilon^m) \ln\left(\frac{\dot{\varepsilon}}{\dot{\varepsilon}_0}\right) + E\dot{\varepsilon}^k. \tag{7}$$

The temperature dependency function used, $f(T)$, is the same as that proposed by Johnson and Cook [21], for which values are taken from the literature.

3.2 Boundary conditions

A challenge in simulating a SHB test, is applying the boundary conditions to the specimen. For a quasistatic test, it is sufficient to apply a displacement boundary condition to the clamped section of the specimen at the same rate as tested. Mass-scaling was used to produce reasonable run times for the quasistatic tests. However, applying velocity boundary conditions directly to a tensile SHB specimen is inaccurate since stress wave reflections will occur at these boundaries that do not occur in the physical apparatus. To avoid this, some researchers model both the input and output bars as well as the specimen and apply the stress pulse measured during testing to the end of the input bar (see Verleysen et al. [22]). However, this method significantly increases the computational time due to the extra elements. An alterna-
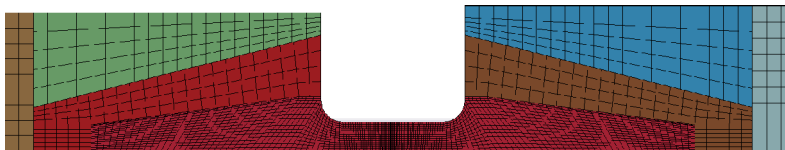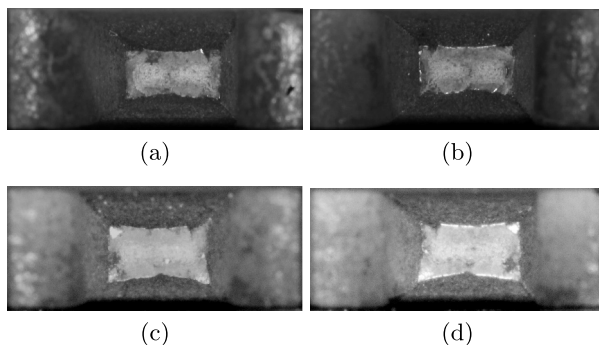
Fig. 5. The SHB finite element mesh.

Fig. 6. Examples of fracture surfaces of straight specimens post-failure. (a) Quasistatic (side A). (b) Quasistatic (side B). (c) Dynamic (side A). (d) Dynamic (side B).

Table 2. The plasticity model constants used for the numerical simulations.

A (MPa)	B (MPa)	C (MPa)	D (MPa)	E (MPa)	$\dot{\varepsilon}_0$ (s^{-1})	n	m	k
301.5	555.4	5.8	5.0	15.0	0.001	0.407	0.45	0.3

tive approach is to model only a small portion of the input and output bars, and use infinite elements [23] at the bar ends in order to prevent reflections of the stress waves. For further detail regarding the implementation of the infinite elements see Weyer [10]. An example of the quarter symmetry SHB model including the bars, clamps, and specimen is shown in Figure 5. The input and output bars were modelled as 200 mm portions which are not shown fully. The measured stress pulse was applied directly to the free end of the input bar, which avoids spurious stress waves cause by applying displacement or velocity boundary conditions.

4 Results

To investigate the effect of strain rate, the fracture surfaces were examined for each specimen. The area of the failure surface is slightly larger for the dynamic test specimens than the quasistatic specimens, as seen in Figure 6, which suggests a decrease in strain at failure.

Force–displacement data was examined numerically to gain a quantitative understanding of the influence of strain rate, as shown in Figure 7.

The topmost curves in Figure 7 represent the SHB experimental data, while the bottom-most curves represent the slowest quasistatic data. The force displacement curves suggest that the material exhibits a decrease in ductility with an increase in strain rate, as well as an increase in strength. Table 2 shows the values obtained for the calibrated plasticity model.
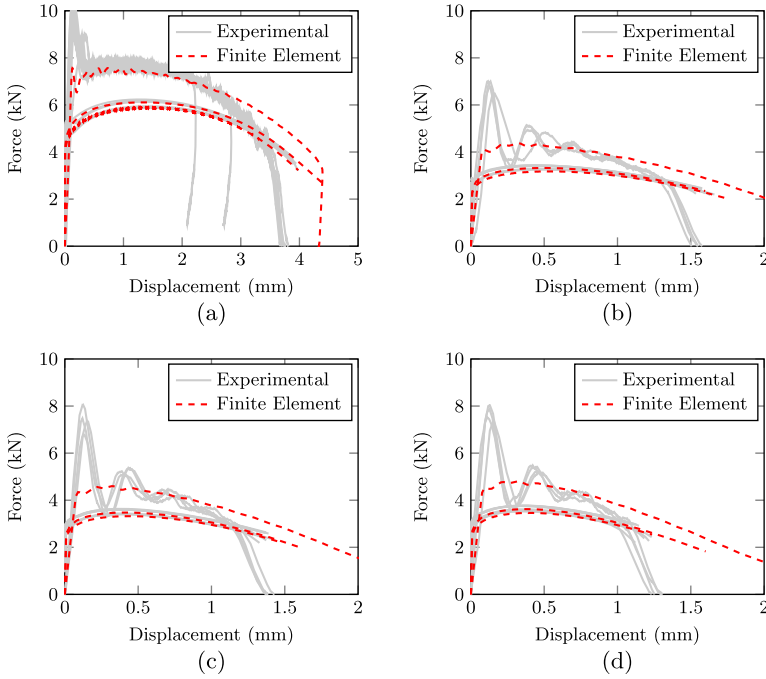
Fig. 7. The experimental and numerical force–displacement data for the different specimens. The curves show an increase in force with an increase in strain rate, with the top curve on each graph representing the SHB data. (a) Straight specimens. (b) R5.0 notched specimens. (c) R2.5 notched specimens. (d) R1.5 notched specimens.

It is difficult to compare the different geometries through a visual examination of the force–displacement curves, as the different notch radii result in different levels of strain localisation, meaning that the variation in displacement is not necessarily an indication of a variation in local strain at failure. This is precisely the reason finite element simulation results are required to determine the local damage parameters at the point of fracture.

5 Damage analysis

Using the calibrated plasticity model, the plastic strain and triaxiality at failure were determined for each unique test. The mesh in the region of necking and fracture was refined to ensure convergence. In the specimen gauge section, there are 30 elements across the thickness, with the shortest element length being 0.075 mm. Figure 8a shows the evolution of Lode angle with time for the R5 notched specimen at 0.6 mm/min. Note that time averaged value of these parameters would differ from the strain averaged value, as calculated by equation (5). Figure 8b shows the strain at failure plotted against the strain-averaged triaxiality for each test. The data was calibrated to a damage function for each of the strain rate regimes, as seen by the three lines on the graph. The chosen damage function is a generalised form of equation (1), given by:

$$\varepsilon_f = D_1 \exp(-D_2\eta). \tag{8}$$

There is a clear indication that ductility decreases as the strain rate increases. By comparing the strain-averaged strain rate for each strain rate regime to the correlated
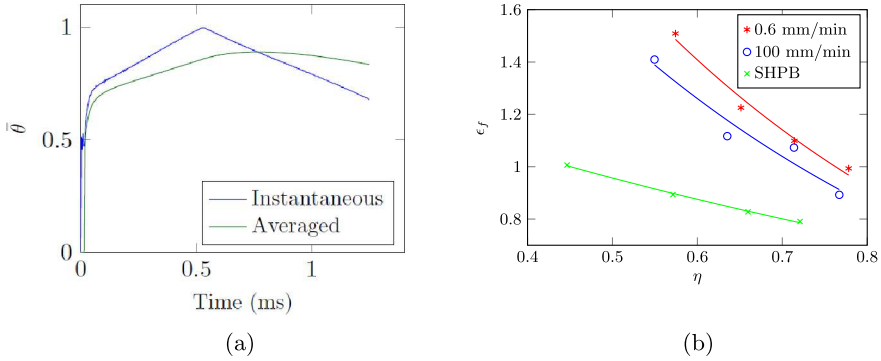
Fig. 8. (a) Lode angle evolution for R5 notched specimen. (b) The plastic strain at failure vs triaxiality for the different strain rate regimes.
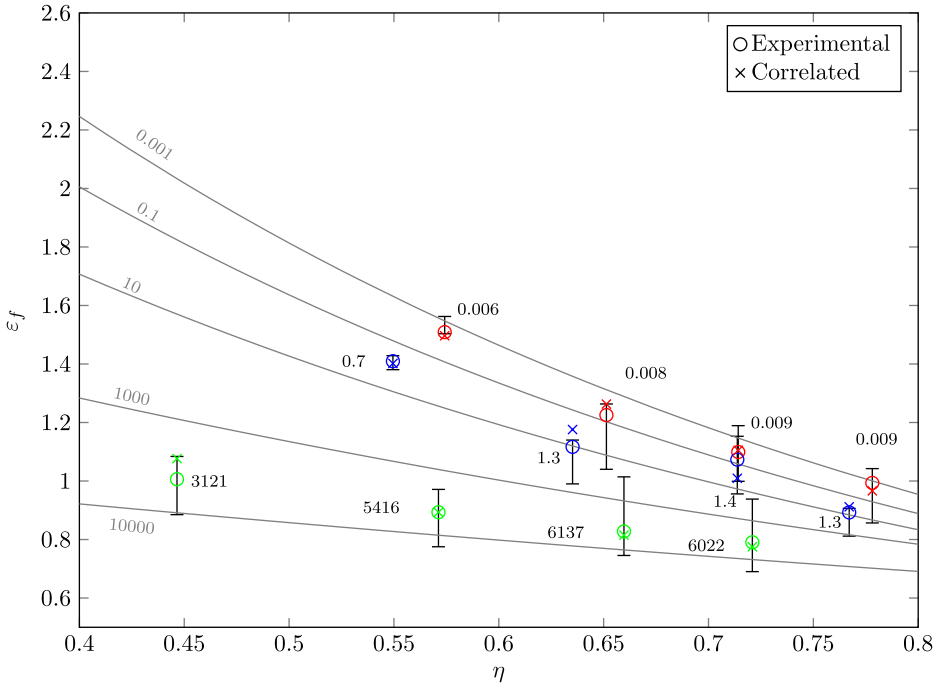

Fig. 9. The plastic strain at failure vs. triaxiality using a strain rate dependent function. The labels represent strain-averaged strain rate in s^{-1}.

constants from equation (8), the plastic strain at failure can be written as a function of strain-averaged triaxiality and strain rate:

$$\varepsilon_f = (D_1 - D_2\dot{\bar{\varepsilon}}^{D_3}) \cdot \exp\left(-(D_4 - D_5\dot{\bar{\varepsilon}}^{D_6})\eta\right), \qquad (9)$$

where $\dot{\bar{\varepsilon}}$ is the strain rate normalised by $\dot{\varepsilon}_0 = 1$.

Figure 9 shows the correlated damage model with strain rate dependence. The experimental data, represented by the circles, were obtained by reading the damage parameters (triaxiality and plastic strain) from the finite element simulation results at the point where the simulated displacement was equal to the measured displacement

Table 3. The correlated parameters for the damage model with strain rate dependency.

D_1	D_2	D_3	D_4	D_5	D_6
7.44	3.39	0.066	2.22	0.28	0.18

at failure. The error bars represent the variance in strain at failure between the test samples. The correlated data, represented by the crosses, was obtained by including the damage model in the same simulations and reading the damage parameters at the time of failure in the simulation. The grey lines represent contours of constant strain rate calculated using equation (9). Table 3 gives the parameters used for the damage model.

As can be seen, the correlated damage model matches the experimental data closely, suggesting that a model using a single function incorporating both the effects of loading conditions and strain rate can be successfully implemented. While it was possible to achieve reasonable agreement between this set of experiments and simulations using a single damage function, it is probable that additional functions would be needed if experiments with a broader range of triaxialities and Lode angles are performed.

6 Discussion

The most noticeable feature in the damage model proposed above, is that the model describes a decrease in ductility with an increase in strain rate, which is in direct contrast with some previous findings from literature [7,11–13]. The data obtained shows a clear inverse relationship between strain rate and strain at failure. This finding suggests that further investigation into this behaviour should be conducted using a wider range of materials and strain rates to determine whether the phenomenon is material specific, and to gain further insight into the relationship between strain at failure and strain rate. The model used to incorporate the effect of strain rate does not have a physical basis, but was rather chosen to yield a good fit to the experimental data. This means that the model is inconsistent at very high strain rates, but was nevertheless useful for quantifying the effect of strain rate on ductile damage for the available data set.

In order to comprehensively study this effect, the research focused on experiments in the range of $\bar{\theta} = 1$ before necking occurs. This means that the above findings cannot necessarily be extended to any loading condition. However, extending the model to include the effect of Lode angle could potentially be implemented by conducting further experiments with specimen geometries which result in lower normalised Lode angles at failure. Furthermore, a need has been identified to obtain more data for strain at failure at varying strain rates. The damage model developed is phenomenological, and was chosen to yield good results over a range of loading condition and strain rates.

7 Conclusions

A novel means of generating a tensile pulse in HPB, with minimal modification to a regular gas gun, was presented. The novel "fir-tree" gripping system for tensile specimens was presented, that permits rapid changing of specimens between tests and provides positive engagement between bar and specimen without requiring very fine tolerances. A variety of notched specimens, machined from DOMEX 355MC,

were tested in tension over a range of strain rates. The high strain rate tensile SHB tests showed consistently higher forces, and lower elongations at fracture, than the quasistatic tests. Parallel finite element simulations were performed to determine the plastic strain and triaxiality at the point of fracture for each unique test. A damage model was correlated to the experimental data incorporating both triaxiality and strain rate dependency. The model yields a good fit over the entire range of tests and is easily implemented in a finite element code. The chosen damage model requires a total of six unique tests to calibrate the parameters, assuming the plasticity model has been calibrated. A significant result is that, in contrast to some existing literature, the damage model indicates a decrease in ductility with increasing strain rate, suggesting that further study into the effect of strain rate on ductile damage is required.

References

1. Y. Bao, T. Wierzbicki, Int. J. Mech. Sci. **46**, 81 (2004)
2. Y. Bai, X. Teng, T. Wierzbicki, Study on the effect of the third stress invariant on ductile fracture, Tech. Rep. 151, Impact and Crashworthiness Laboratory, Massachusetts Institute of Technology, Cambridge, MA, 2006
3. Y. Bai T. Wierzbicki, Int. J. Plast. **24**, 1071 (2008)
4. F. McClintock, J. Appl. Mech. **35**, 363 (1968)
5. J. Rice, D. Tracey, J. Mech. Phys. Solids **17**, 201 (1969)
6. A.L. Gurson, J. Eng. Mater. Technol. **99**, 2 (1977)
7. G.R. Johnson, W.H. Cook, Eng. Fract. Mech. **21**, 31 (1985)
8. L. Xue, T. Wierzbicki, Eng. Fract. Mech. **75**, 3276 (2008)
9. Y. Bai, T. Wierzbicki, Eng. Fract. Mech. **135**, 147 (2015)
10. M. Weyer, An experimental and theoretical study on the effect of strain rate on ductile damage, Master's thesis, University of Cape Town, 2016
11. A.H. Clausen, T. Børvik, O. S. Hopperstad, A. Benallal, Mater. Sci. Eng. A **364**, 260 (2004)
12. B. Erice, F. Gálvez, D. Cendón, V. Sánchez-Gálvez, Eng. Fract. Mech. **79**, 1 (2012)
13. A.S. Khan, H. Liu, Int. J. Plast. **37**, 1 (2012)
14. C.C. Roth, D. Mohr, Int. J. Plast. **56**, 19 (2014)
15. T. Børvik, O. Hopperstad, T. Berstad, M. Langseth, Eur. J. Mech. A: Solids **20**, 685 (2001)
16. P. Verleysen, J. Peirs, Int. J. Impact Eng. **108**, 370 (2017)
17. R. Curry, G. Langdon, Int. J. Impact Eng. **102**, 102 (2017)
18. S.C.K. Yuen, G. Langdon, G. Nurick, E. Pickering, V. Balden, Int. J. Impact Eng. **46**, 97 (2012)
19. Y. Bao, T. Wierzbicki, Eng. Fract. Mech. **72**, 1049 (2005)
20. H. Zhao, Mater. Sci. Eng. A **230**, 95 (1997)
21. G.R. Johnson, W.H. Cook, in *Proceedings of the 7th International Symposium on Ballistics* (The Hague, The Netherlands, 1983), Vol. 21, pp. 541–547
22. P. Verleysen, B. Verhegghe, J. Degrieck, B. De Cooman, *WIT Transactions on Engineering Sciences*, edited by M. Alves, N. Jones, (WIT Press, 2005), pp. 549–562
23. J. Lysmer, R.L. Kuhlemeyer, J. Eng. Mech. Div. **95**, 859 (1969)